Journal of Molecular Liquids 420, 126814 (2025) DOI: https://doi.org/10.1016/j.molliq.2024.126814

Controlling diffracted beam-polarization by patterned optical-field in a photosensitive chiral nematic

Fei Liang,[1] Hongzhen Jing,[1] Jiaming Fu,[1] Ying Xiang[1*]
[1]School of Information Engineering, Guangdong University of Technology, Guangzhou 510006, People's Republic of China

Péter Salamon,[2*] Nándor Éber,[2] Ágnes Buka[2]
[2]HUN-REN Wigner Research Centre for Physics, 1525 Budapest, P.O.Box 49, Hungary

Michal Kohout[3]
[3]Department of Organic Chemistry, University of Chemistry and Technology Prague, Technická 5, CZ-16628 Prague, Czech Republic

Jiaoyang Li[4]
[4]National Demonstration Center for Experimental Physics Education, School of Physics, Sun Yat-Sen University, Guangzhou 510275, China

Jiawen Chen[5]
[5]National Center for International Research on Green Optoelectronics, South China Normal University, Guangzhou 510006, People's Republic of China

*Corresponding authors:
frank_xiang68@qq.com; salamon.peter@wigner.hun-ren.hu

Abstract: Rotation of the light polarization of a diffracted beam, manipulated by imposed patterned UV optical field, is proposed and examined in a photosensitive chiral nematic liquid crystal. Such operations can be performed dynamically and reversibly, by varying the UV intensity. It was revealed that the rotations are ascribed to an optical-field-induced chirality effect, where the helical structure in chiral nematics changes periodically in space in accordance with the UV intensity profile. Using continuum elastic theory and the optical Jones matrix technique, we determined the dependence of polarization orientation on UV intensity. By changing the polarity and magnitude of chirality in chiral nematics, UV light can control the orientation of the polarization state sweeping across the entire horizontal plane, making it possible for polarization converter applications. Proof-of-concept prototypes capable of generating customized vortex and vector beams are demonstrated, proving that by virtue of remote and precise control of the optical field, a polarization field with specific spatial structures can be generated.

Keywords: Cholesteric Liquid Crystals, Self-Assembly Microstructures, Stimuli-Responsive Materials, Optically-induced Grating, Light Polarization, Phototuning

1. Introduction

Nematic liquid crystals (NLCs) and their chiral counterparts, chiral nematics or cholesterics (CLCs) are intriguing soft materials, sharing some typical properties of both liquids and crystals. Thanks to their self-assembling ability, optical anisotropy and sensitivity to the external fields, nematics are widely exploited in photonic devices to perform specific functionalities [1-2].

One important optical application of nematics (whether achiral or chiral) is the fabrication of diffraction gratings. This can be achieved by various methods, such as: (a) using structured electrodes, the deformation profile of nematics is in accordance with the morphologies of the applied periodic electric fields [3]; (b) employing periodic alignment, usually adopting a photoalignment technique, where a layer of azo-dye acts as a substrate for the nematic and the *trans-cis* conformation change of the dye under polarized UV light alters the alignment, resulting in a periodic deformation of nematics [4]; (c) exploiting a patterned optical field specific spatial and temporal reorientation of nematics can easily be acquired, resulting in dynamic optically-induced gratings [5-6]; (d) taking advantage of the self-assembling capability, e.g. occurrence of electroconvection associated with electric current and fluid flow, or flexodomains characterized with a periodically deformed equilibrium state, nematics can spontaneously form gratings, whose morphologies mainly depend on the electric transport parameters of the NLC material [7-9].

Compared with other kinds of gratings, the most captivating characteristics of nematic gratings (especially of those of cases (c) and (d)) is their reconfigurable capacity. Their morphologies can be manually tailored, thus making them good candidates for monochromator, spectrometer, optical fibre telecommunication, laser projection applications. Nematic gratings have already shown excellent performance on dynamically controlling the optical phase, amplitude and diffraction efficiency.

However, with the emergence of new optical technologies, such as utilizing optical vortices and vector light fields, having potential applications in the fields of optical communication, polarization imaging, biomedical analysis and materials characterization, the demand of controlling the light parameters is being extended from the traditional intensity, frequency and phase to the actual polarization state.

For a long time, nematics have been found ideal candidates to tune the light polarization state of transmitted light [10-11]. Usually, in a twisted nematic device, where the director rotates along the substrate normal, the electric vector of the transmitted light follows the rotation of the director synchronously and the corresponding polarization state changes accordingly [12-13]. It should be noted, however, that while most previous works focused on the modulation of transmitted light, in some cutting-edge scenarios, for example augmented/virtual reality (AR/VR) application, the rotation of the polarization of diffracted light in a dynamic manner would be essential [14-15].

As a common solution, nematic polarization gratings (PGs) were exploited to manipulate the polarization state of diffracted beams. PGs were often fabricated by photo-alignment technique, where substrates were treated by light possessing a polarization pattern, created by orthogonal circularly-polarized beams, thus the nematic director was periodically distributed in the substrate [16]. Such gratings demonstrate peculiar polarization characteristics: when a linear-polarized probe beam is incident, the diffraction pattern exhibits, besides the transmitted beam (0^{th} order), only the $\pm 1^{st}$ diffraction orders, which retain equal intensities and opposite circular polarizations. Furthermore, if the incident light is left- (or right-) circularly polarized, from the diffracted spots only the $+1^{st}$ (or -1^{st}) order is present, depending on the handedness of the circular polarization [17-18]. PGs can direct a polarized incident beam into multiple pairs of orthogonally polarized diffracted beams, however, their device structure as well as their surface anchoring is permanent and irreversible; thus this polarization conversion is fixed and not alterable.

Herein, in order to manipulate the polarization of diffracted light dynamically and smoothly, an optically-induced grating composed of a light sensitive cholesteric liquid crystal — a nematic with a photosensitive chiral dopant — is introduced. Stimulated by an applied patterned optical field, helical structures with different pitch and chirality emerge alternately in space, forming a grating that diffracts the incident light beam. It was observed that the polarization state of the diffracted beam depends on the intensity of the commanding optical field. In addition, in order to make such polarization rotation continuous, a hybrid aligned cholesteric (HAC) cell was adopted to ensure the change of helical pitch freely, not being constrained by the bounding surface. With the optimized combination of the chiral nematic pitch and the UV intensity range, the corresponding polarization rotation angle can sweep over the whole horizontal plane (from $-\pi/2$ to $+\pi/2$).

This idea can be generalized to define arbitrary spatial polarization distribution according to custom presettings, with dynamically and in situ switchable tunability. It is anticipated that such a light-polarization manipulated diffraction device, accompanied by stimuli-responsive reconfiguration of cholesterics, will open a new concept of the light-directing soft superstructures with a charming prospect on materials, photonics and applications.

2. Materials and Methods

2.1 Samples

The measurements were performed on a CLC obtained by doping a nematic host E7 with the chiral dopant M5 (9-(2-methyl-2,3-dihydro-1H-cyclopenta[a]naphthalen-1-ylidene)-9H-fluorene) [8, A] at weight concentration C_{M5}. The host E7 is a multicomponent nematic mixture of Merck, composed of 51% of 5CB (4-cyano-4'-n-pentyl-1,1'-byphenyl), 25% of 7CB (4-cyano-4'-n-heptyl-1,1'-byphenyl), 16% of 8OCB (4-cyano-4'-n-octyloxy-1,1'-byphenyl) and

8% of 5CT (4-cyano-4''-n-pentyl-1,1',1''-terphenyl) [B, C]. The chemical structures of the dopants M5(L) and M5(R) are shown in Figs. 1(a) and 1(b).

M5 exists in the form of two antipodes: M5(R) induces right-handed cholesteric helix, while M5(L) results in a left-handed helix. The chiral dopant M5 behaves as a photosensitive molecular switch; its helical twisting power (*HTP*) varies with the intensity of the UV irradiation, resulting in a tunable helical pitch $P(I_{uv})$ [8]. It was found that for each concentration there is a critical UV intensity (e.g. I_c = 1.25 mWcm^{-2} at C_{M5} = 0.0067%), where the *HTP* becomes zero, i.e. the helical structure fully unwinds yielding a nematic-like, compensated cholesteric state with $|P(I_c)| = \infty$. Taking M5(R) as an example: initially, without UV illumination, M5(R) induces ***right-handed*** cholesteric helix; then upon UV illumination, M5(R) molecules may undergo photoisomerisation; if the UV intensity exceeds I_c, the helix switches to an opposite (***left-handed***) helical sense.

In order to perform measurements, the CLC compound was filled into HAC cells with thickness *d*, where one substrate surface was treated by the Nissan 7511L polyimide to obtain homeotropic alignment, while the other substrate was covered by the Nissan SE150 polyimide, which resulted in a parallel alignment after rubbing along the direction $\mathbf{n_0}$ [20].

2.2 The photo-tuning setup

Using a digital micro-mirror device (DMD), a dynamic mask photo-tuning technique was employed (Fig. 1), where pattern images, with a one-dimensional binary periodic structure, were uploaded as photomasks. Here the periodic unit possessed two parts of equal width, where one part was always in the dark state, which led to no reflection of UV, while the other part was in a uniform grey state, which gave rise to reflection of UV whose intensity I_{uv} depended on the grey level.

A collimated UV beam (with wavelength λ = 365 nm), whose intensity was detected by an UV meter placed in front of the sample, acted as commanding light, which was reflected onto the DMD and subsequently carried the designed light intensity pattern. The sample was shone by this periodic intensity light, which formed a grating, whose morphology was monitored by a CCD camera, when collimated white light and polarizers were adopted [21]. Meanwhile, a linearly polarized laser (λ = 633 nm) acted as the probe beam that impinged upon the sample, and the polarization state of the produced diffracted beam was measured by a polarimeter (PAX1000 from THORLABS). In addition, optical color filters were installed before the polarimeter, the photodetector and the CCD to block the UV light.

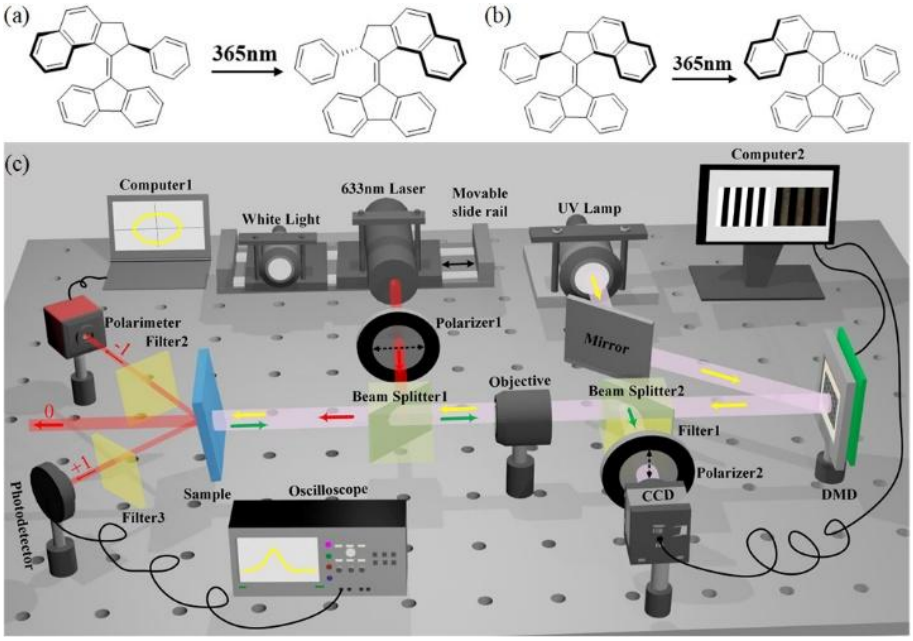

Figure 1. Molecular structure of (a) the chiral dopant M5(L) and (b) the chiral dopant M5(R) in dark state and after photoisomerization by UV light. (c) Schematic diagram of the DMD-based dynamic mask system for photo-tuning, which integrated light emission, dynamic pattern generation, image focusing and monitor components.

3. Experimental results

In most of the following experiments, a sample with $C_{M5(L)}$ = 0.0067% of initially *left-handed* M5(L) and d = 100 μm was used. This combination of $C_{M5(L)}$ and d was selected to produce the unperturbed twist angle ($\Phi_0 \approx -\pi$) of the director at I_{uv} = 0, which made the polarization of the transmitted beam rotate –π with respect to that of the incident beam. With such sample, it was observed that the polarization of the 1st order diffracted beam can rotate +π/2 with respect to that of the incident beam, if the applied I_{uv} is strong enough. Meanwhile, a patterned UV field with periodicity of Λ = 100 μm and different intensities ($I_{uv} \geq I_c$) was prepared in order to examine the change of the polarization states of the 1st order diffracted beam.

3.1 Evolution of the spatial helix and the induced periodic structure

When the sample was subjected to patterned UV light of laterally alternating intensity, a spatially periodic helical structure developed, whose pitch and chirality varied in accordance with the intensity profile of the commanding UV light. Herein with $I_{uv} > I_c$, the grating formed as a regular array of alternating stripes of a *right-handed* helical structure with $P = +P_2 > 0$ and a *left-handed* helical structure with $P = -P_0 < 0$. The latter always stayed in the *initially left-handed* state due to the absence of UV light, while the former changed into different *right-handed* states with individual $+ P_2(I_{uv})$ due to exposure to an adjustable UV light, as shown in Fig. 2.

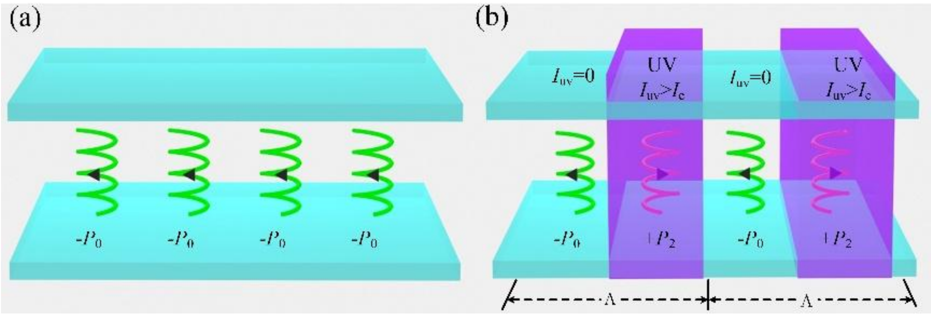

(old version)

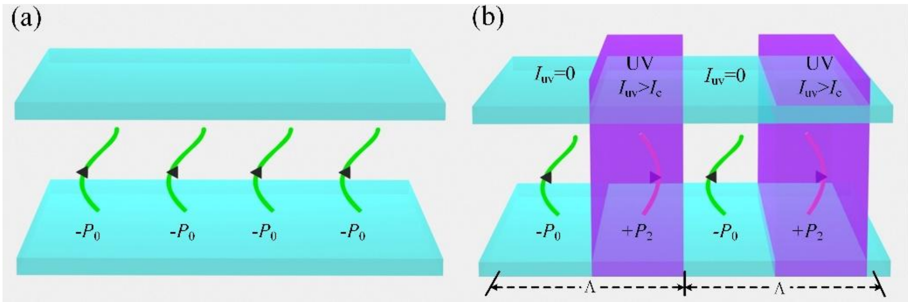

Figure 2. Schematic diagram of spatially distributed helical structures upon patterned UV light with periodicity Λ and intensity I_{uv}. (a) The sample is in the *initially left-handed* state with uniform pitch $-P_0 < 0$ at $I_{uv} = 0$; (b) the sample remains in the *initially left-handed* state with pitch $-P_0$ in the dark (unilluminated) areas, whereas in the bright (illuminated) areas, the sample turns into a *right-handed* state with pitch $+P_2 > 0$ at $I_{uv} > I_c$. [Comment_EN: Though I liked this figure, due to referee's request I suggest to redraw, keeping only one half turn of the director, which would correspond to the typically used geometry.]

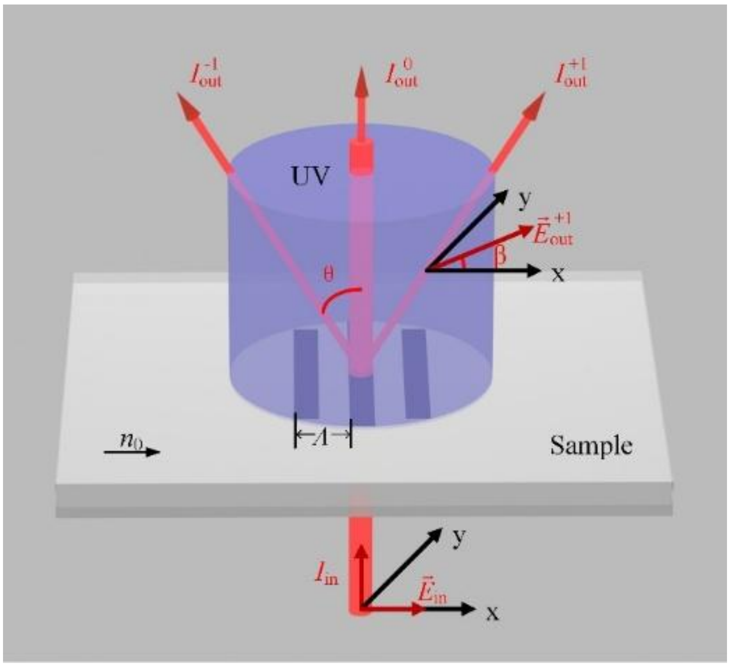

Figure 3. Schematic diagram of diffraction effect of the chiral grating formed by spatially periodic varying helical structures with periodicity Λ, steered by an additional patterned UV light. I_{in} and $\mathbf{E_{in}}$ are the intensity and polarization state of the incident beam, I_{out}^{+1} and $\mathbf{E}_{\mathbf{out}}^{+1}$ are the intensity and polarization state of the +1st order diffraction beam. Angle β describes the rotation of the polarization with respect to that of the incoming beam.

With alternating pitch values $-P_0$ and $+P_2(I_{uv})$, the helical structures vary periodically in the cell plane, and diffract the normally incident light beam, as shown in Fig. 3. Due to the couplings among the longitudinal helix, the transverse periodic structure and the incident beam, the characteristics of the diffracted beam, such as the polarization state and the diffraction intensity, all depend on the intensity profile of the commanding UV field. Therefore, we explored how I_{uv} affects the morphology of the sample, the intensity (the efficiency η) of the diffracted beam and its polarization state. The latter includes the degree of linear polarization defined as $DoLP = (I_{major} - I_{minor})/(I_{major} + I_{minor})$, where I_{major} and I_{minor} are the intensities along the major and the minor axes of the elliptically polarized beam, respectively. $DoLP = 1$ means a perfectly linearly polarized state.

3.2 Effect of the patterned UV intensity on the CLC textures

Under the illumination of patterned UV light, patterned morphology developed in samples, characterized by well-defined stripes textures. Not only the colour and contrast of the textures change with I_{uv}, but the corresponding intensity and polarization state of the diffracted beam varies as well, as demonstrated by Figs. 4(a(1))–4(d(1)), 4(a(2))–4(d(2)), 4(a(3))–4(d(3)), respectively. Increasing the UV intensity reduces the contrast of the pattern, and the relative intensity of the diffracted fringes, but enlarges the angle of polarization rotation.

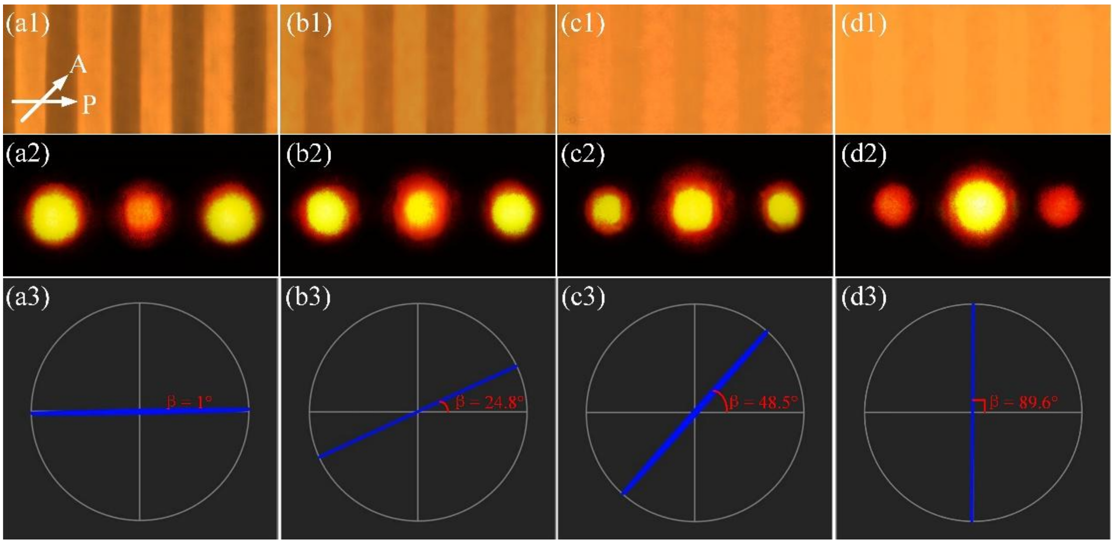

Figure 4. Polarization state of the ±1st order beam diffracted on the chiral grating formed by illumination with a patterned UV field with various intensities in an initially left-handed sample with twist angle $\Phi_0 \approx -\pi$ ($C_{M5(L)} = 0.0067\%$). The columns (a)-(d) correspond to $I_{uv} = 1.5\ I_c$, $I_{uv} = 2.0\ I_c$, $I_{uv} = 3.6\ I_c$ and $I_{uv} = 16.8\ I_c$, respectively. The rows (1), (2) and (3) show representative snapshots (450×290 μm) of the texture, the diffraction fringes and the polarization state of the ±1st order diffraction beam, respectively.

3.3 Effect of the patterned UV intensity on the rotation of the polarization of the diffracted beam

Upon patterned UV light, diffraction fringes emerge gradually. We measured the diffraction angle ψ of diffraction spots (1st order) and estimated the corresponding grating constant Λ_g from the equation $\Lambda_g = \frac{\lambda_{633nm}}{\sin\psi}$. Comparing Λ_g with the periodicity Λ of the patterned UV intensity, we found that $\Lambda_g = \Lambda$ always holds, even if Λ was adjusted by different photomasks. This coincidence proves that the chiral grating inside the sample is produced by the patterned UV field.

When the incident beam was linearly polarized along the *x* axis, the polarization state of the diffracted beam (±1st order) was observed to remain always linear during the change of I_{uv}, while the corresponding polarization angle β varied according to I_{uv}. Namely, upon enhancing I_{uv}, β increased monotonically and continuously from $\beta = 0$ to $\beta = +\pi/2$ by ***rotating anti-clockwise***, as shown in Fig. 5.

In addition, β could be changed reversibly by adjusting I_{uv}, without any hysteresis. For example, β decreased with lowering I_{uv}, and eventually returned to $\beta = 0$ at I_c.

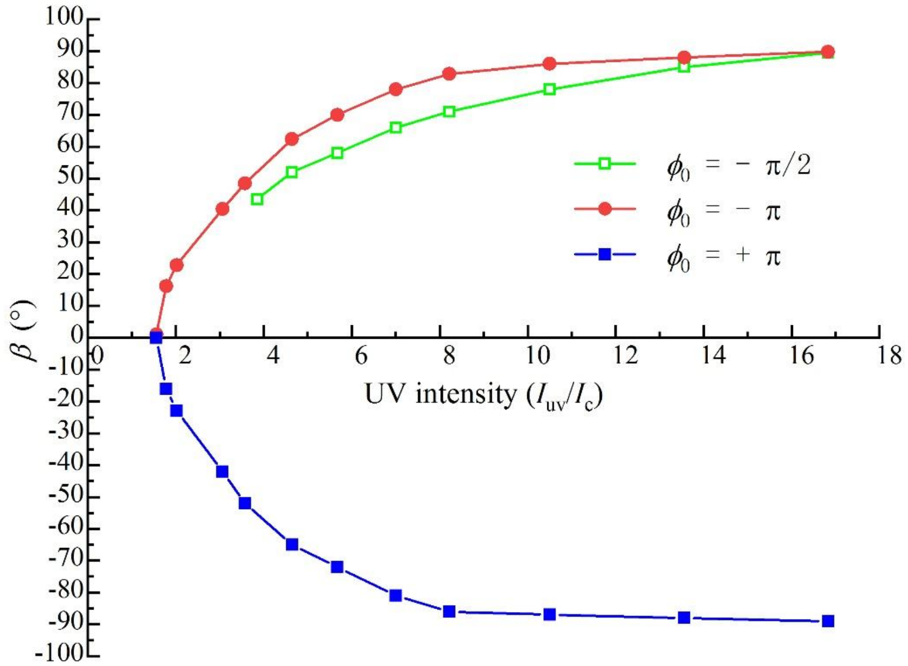

Figure 5. Dependence of the polarization angle β of the diffracted beam (1st order) on UV intensity I_{uv} in different samples: initially right-handed sample with twist angle $\Phi_0 \approx +\pi$ ($C_{M5(R)}$ =0.0067%, solid blue square), initially left-handed sample with twist angle $\Phi_0 \approx -\frac{1}{2}\pi$ ($C_{M5(L)}$ = 0.0037%, open green square) and initially left-handed sample with twist angle $\Phi_0 \approx -\pi$ ($C_{M5(L)}$ = 0.0067%, solid red circle), respectively. The range of I_{uv}/I_c was selected in order to fulfil *DoLP* ≥ 0.99 at acceptable diffraction intensity $\eta > 5\%$.

The diffraction efficiency η was also affected by the intensity I_{uv} of pattern UV light. Here η is defined as the ratio of the intensity of the ±1st order diffracted beam to the intensity of the incident beam. Interestingly, η grows with increasing I_{uv} in the sample with $\Phi_0 \approx -\frac{1}{2}\pi$, but diminishes in the sample with $\Phi_0 \approx -\pi$ (Fig. 6).

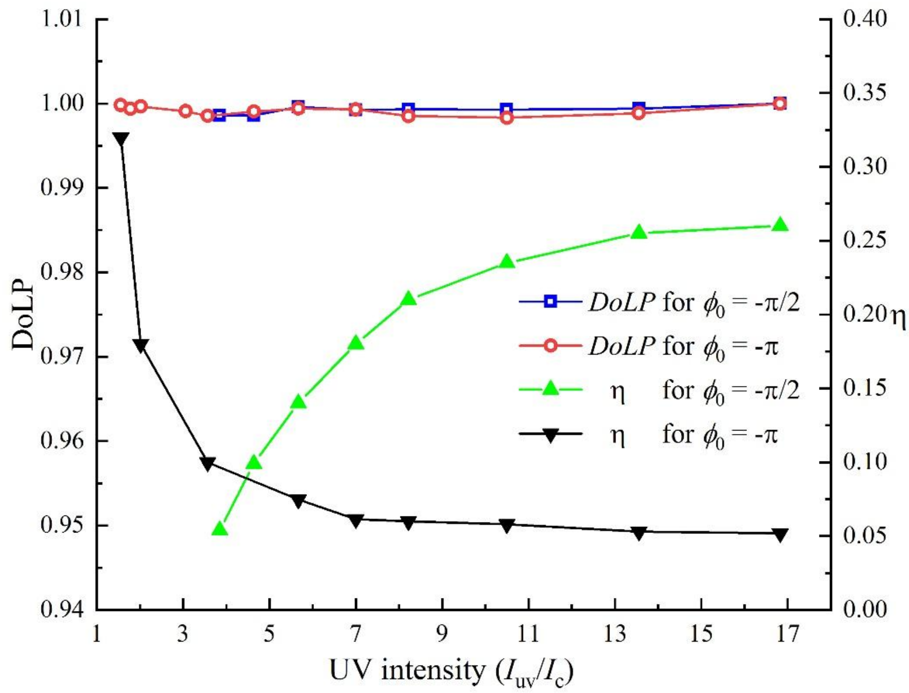

Figure 6. Dependence of *DoLP* and η on the UV intensity I_{uv}, in the initially left-handed sample with twist angle of $\Phi_0 \approx -\pi$ ($C_{M5(L)}$ = 0.0067%, open red circle and black down triangle) and in the initially left-handed sample with twist angle of $\Phi_0 \approx -\frac{1}{2}\pi$ ($C_{M5(L)}$ = 0.0037%, open blue square and green up triangle).

Meanwhile, the variation of *DoLP* of the diffracted beam was examined depending on the I_{uv}, as shown in Fig. 6. It was found that the *DoLP* indicates a reasonably high degree of linear light polarization during the whole adjustability range of $-\pi/2 \leq \boldsymbol{\beta} \leq +\pi/2$.

3.4 Effect of the chiral dopant concentration on the photo-tuning operation

While the adjustability range of β could be determined by I_{uv}, further inspection indicated that it also depends on the magnitude of chirality. Herein, an additional sample with $C_{M5(L)}$ = 0.0037%, whose unperturbed twist angle would be $\Phi_0 \approx -\frac{1}{2}\pi$ at $I_{uv} = 0$, was examined to explore the connection between β and C_{M5}. Under this situation, no matter how large I_{uv} was used, the rotation range of polarization was limited approximately to between $+\pi/2$ and $+\pi/4$ ($\frac{\pi}{4} \lesssim \beta \lesssim \frac{\pi}{2}$), as shown in Fig. 5 and Fig. 7. In general, the rotation angle was larger in samples with higher concentration of the chiral dopant. Namely, the larger $|\Phi_0|$, the larger the range of β.

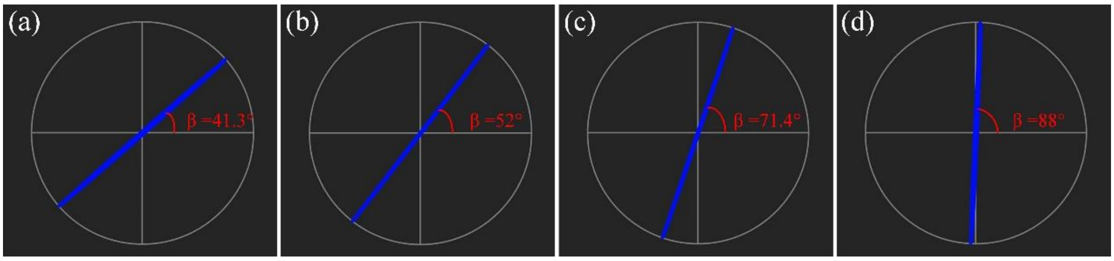

Figure 7. The dependence of the polarization angle β of the diffracted beam (1st order) on the UV intensity I_{uv} in the $\Phi_0 \approx -\frac{1}{2}\pi$ sample. Columns (a) - (d) correspond to I_{uv} = 3.6 I_c, I_{uv} = 4.6 I_c, I_{uv} = 8.2 I_c and I_{uv} = 16.8 I_c, respectively.

3.5 Effect of the sign of chirality on the adjustable range of polarization

Although β could be adjusted by I_{uv} between +π/2 and 0 in the ***initially left-handed*** sample of $\Phi_0 \approx -\pi$ (Fig. 4), from the view point of practical application, adjustability range of $-\frac{\pi}{2} < \beta < +\frac{\pi}{2}$ would be essential, which could guarantee the rotation of polarization to scan the whole horizontal plane. Therefore, samples with opposite handedness, i.e., ***initially right-handed*** ones, were examined to extend the range of β. For comparison, a sample with $C_{M5(R)}$ =0.0067% of M5(R) and d = 100 μm was chosen in order to produce a symmetrical unperturbed twist angle ($\Phi_0 \approx +\pi$) at I_{uv} =0.

It was observed that the behavior of the two complementary samples (those with $\Phi_0 \approx -\pi$ and $\Phi_0 \approx +\pi$) are very similar, except that their rotation angles are of opposite sign due to the different handedness of the twist structures, as shown in Fig. 5. Thus, with a properly selected combination of the UV intensity I_{uv}, dopant concentration C_{M5} and dopant type (M5(L) or M5(R)), an arbitrary rotation of the linear polarization of the diffracted beam could be achieved.

4 Discussion:

The aforementioned experimental results demonstrate that the UV light irradiation rotates the polarization plane of diffracted beam via alteration of the helical pitch, where the magnitude and direction of the rotation angle depend on the UV light intensity, on the concentration and on the type of the chiral dopant.

It should be noted that usually, in conventional NLC gratings, only the diffraction intensity was changeable under stimulation with external fields, thus herein, the observation of adjustable polarization of the diffracted beam is a quite unexpected feature.

4.1 Formation of spatially periodic pitch upon *patterned* UV field

In the HAC geometry, the sample acquires a helical structure with the helical axis perpendicular to the substrates and the tilt angle of the director changes continuously from planar to homeotropic. It corresponds to a twisted nematic system, where the pitch $P(I_{uv})$ can change due to the photo-induced chirality effect of the photosensitive chiral dopant. Meanwhile, without an azimuthal constraint at the homeotropic surface, $P(I_{uv})$ can be tuned freely by I_{uv}; consequently the total twist angle can change smoothly from Φ_0 to $\Phi(I_{uv})$, depending on the ratio of $d/P(I_{uv})$.

Initially, it is assumed that two structures coexist in the sample: one is the lateral periodic structure produced forcibly by the external patterned UV illumination, the other is the longitudinal helical structure formed by an internal molecular self-assembling effect along the substrate normal. Though the above two structures grow in different directions, their morphologies are connected by the spatial distribution of chirality sign and pitch, which depend on the UV intensity profile.

It is a straightforward conclusion that the observed diffraction mainly results from the periodic pitch modulation between the exposed and unexposed areas: at the exposed areas, the pitches develop according to I_{uv}; whereas at the unexposed areas, the pitches are invariable. Consequently, the polarization behavior of the diffracted beam depends on the competition between neighboring helical structures.

The reason why the polarization states of the diffracted beams are linear, and how to interpret the dependence of polarization angle β on I_{uv} will be interesting topics for further research. At present, as a first step, we will conduct numerical simulation to review such effect.

4.2 Simulation of the diffraction behavior

a) *Deformation in the stripes*

The sample can be regarded as a system composed of two alternating individual stripes with $\Lambda/2$ width corresponding to the UV-unexposed dark and the UV-exposed grey areas. Let us consider one period of the periodic structure: at $-\Lambda/4 < x < +\Lambda/4$ with the cholesteric pitch $-P_0$ for the unexposed region and at $-\Lambda/2 < x < -\Lambda/4$ and $+\Lambda/4 < x < \Lambda/2$ with $P(I_{uv})$ for the UV exposed part. Assuming homogeneously unexposed (dark) or UV illuminated cases, the director field is described by the $\phi(z)$ azimuthal and $\theta(z)$ tilt angles; here, within the stripes, all angles depend on the coordinate z (normal to the substrates) only and were recently calculated from the continuum theory [13]. By implementing the previously established continuum theory for the homogeneous case, we calculated the total twist angle $\Phi = \phi(z = d)$ of the director as a function of the pitch-to-thickness ratio P/d as seen in Fig. 8. It follows from the curve that $\Phi_0 = -\frac{1}{2}\pi$ requires $-P_0 = -2.523\ d$, while $\Phi_0 = -\pi$ occurs at $-P_0 = -1.476\ d$.

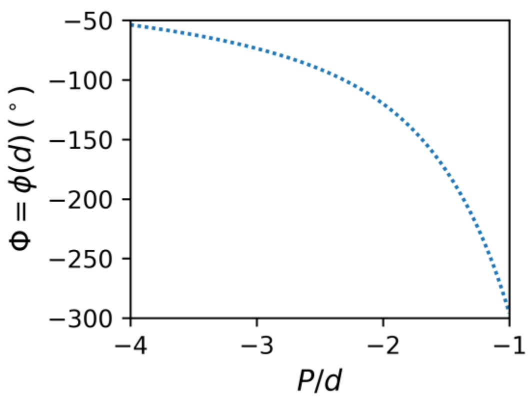

Figure 8. Total twist of the director calculated as a function of the pitch-to-thickness ratio.

The simplest idea to describe the stripe structure induced by the periodic UV exposure is to assume homogeneous director (calculated by the continuum theory for the homogeneous case) within the illuminated and unexposed regions for distinct P_{UV} and $-P_0$ pitches, respectively. In this assumption, the director distribution within each stripe is constant, resulting in a step-like transition at the border of two neighbouring stripes (at $x = \pm\Lambda/4$). In the following, we refer to this approach as the one-dimensional (1D) approximation.

Though the alternating pitch is a precondition due to the UV illumination through a mask, a sharp, discontinuous transition of the director field (and the pitch) might be non-realistic; instead, the continuum theory requires a smoothly changing director, as that would minimize the system's free energy. For this reason, we attempted to extend the calculation taking into account the additional *x* dependence of the director, yielding $\phi(x,z)$ and $\theta(x,z)$. In this case, the free energy density of the sample reads as

$$\begin{aligned} f = \frac{1}{2}K_2\left(q_0 - \cos^2\theta\,\frac{\partial\phi}{\partial z} - \sin\phi\,\frac{\partial\theta}{\partial x} + \frac{1}{2}\cos\phi\,\sin2\theta\,\frac{\partial\phi}{\partial x}\right)^2 \\ + \frac{1}{2}K_1\left(\cos\phi\,\sin\theta\,\frac{\partial\theta}{\partial x} + \cos\theta\left(-\frac{\partial\theta}{\partial z} + \sin\phi\,\frac{\partial\phi}{\partial x}\right)\right)^2 \\ + \frac{1}{2}K_3\left\{\sin^2\theta\left(\frac{\partial\theta}{\partial z}\right)^2 + \cos\phi\,\sin2\theta\,\frac{\partial\theta}{\partial z}\,\frac{\partial\theta}{\partial x}\right. \\ \left. + \cos^2\theta\left[\cos^2\phi\left(\frac{\partial\theta}{\partial x}\right)^2 + \left(\sin\theta\,\frac{\partial\phi}{\partial z} + \cos\theta\,\cos\phi\,\frac{\partial\phi}{\partial x}\right)^2\right]\right\} \end{aligned} \quad (1)$$

Minimization by Euler-Lagrange equations yields two coupled partial differential equations for $\phi(x,z)$ and $\theta(x,z)$, which have been attempted to be solved numerically using COMSOL. Periodic boundary conditions were used for the boundaries at $x = -\Lambda/2$ and $x = +\Lambda/2$, while strong anchoring with $\theta = 1^\circ$, $\phi = 0$ at $z = 0$, and $\theta = 89^\circ$ at $z = d$ were assumed. The total twist angle of the director $\Phi(x) = \phi(x,d)$ is a result of the calculations. During the simulations the material parameter set of Ref. [13] was used. In the following, we refer to this approach as the two-dimensional (2D) approximation.

Calculations have successfully been performed for the sample with $\Phi_0 = -\frac{1}{2}\pi$ ($-P_0 = -2.523\ d$). Figures 9(a) and 9(b) show the calculated tilt $\theta(x,z)$ and twist $\phi(x,z)$ angles of the director, respectively, assuming that in the UV-illuminated stripe $+P_2(I_{uv}) = +P_0 = +2.523\ d$. The figures clearly indicate that the angles are not symmetric with respect to the centers of the stripes ($x = 0$ and $x = \Lambda/2$). This asymmetry is attributed to the pretilt at the planar side. Changing the sign of the pretilt angle results in reversing of the direction of the asymmetry. In Fig. 10, we compare the total twist angle $\Phi(x) = \phi(x,d)$ of the director provided by the 1D and the 2D models. It demonstrates that due to the continuous director transition at the stripe boundaries in the 2D model, the maximal total twist angle is considerably reduced compared to its value in the 1D model.

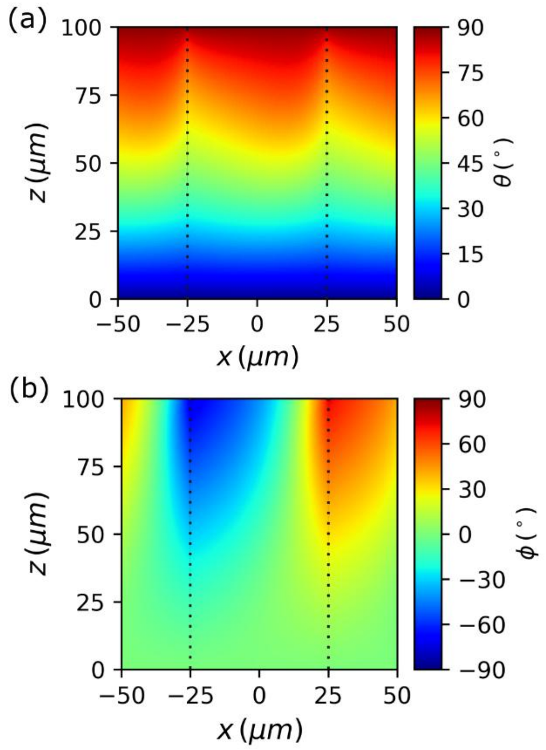

Figure 9. Plots of the calculated $\theta(x,z)$ and $\phi(x,z)$ for the sample with $\Phi_0 \approx -\frac{1}{2}\pi$. Unilluminated stripe: $-25\ \mu m \le x \le 25\ \mu m$, $-P_0 = -2.523\ d$; UV-illuminated stripe: $-50\ \mu m \le x \le -25\ \mu m$ and $25\ \mu m \le x \le 50\ \mu m$, $P_2(I_{uv}) = +P_0 = +2.523\ d$. The vertical dashed lines mark the stripe boundaries.

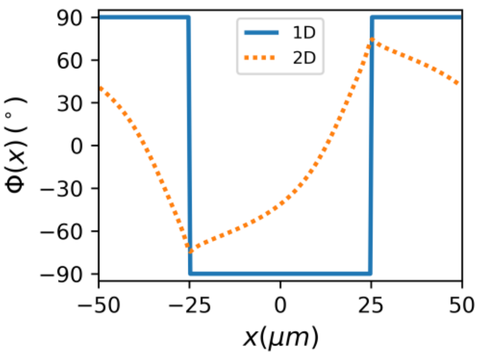

Figure 10. Comparison of the total twist angle *Φ(x)* of the director obtained in the 1D (solid line) and the 2D (dotted line) models. Unilluminated stripe: –25 μm ≤ x ≤ 25 μm, $-P_0 = -2.523\ d$; UV-illuminated stripe: –50 μm ≤ x ≤ –25 μm and 25 μm ≤ x ≤ 50 μm, $P_2(I_{uv}) = +P_0 = +2.523\ d$.

b) *Optical characteristics of the stripes*

Knowing the deformation profile, the optical properties of the sample were calculated by the Jones matrix technique [22].

In the 1D model, due to the binary periodic structure, only two Jones matrices, $\mathbf{J}_{\mathrm{dark}}$ and $\mathbf{J}_{\mathrm{UV}}$, representing the dark and grey areas, respectively, are involved. Both $\mathbf{J}_{\mathrm{dark}}$ and $\mathbf{J}_{\mathrm{UV}}$ are assumed to be uniform and independent of the transverse displacement x; however, they vary along z. In order to handle the helical structure, each stripe was divided into a stack of N layers along the z direction (helical axis). Each layer of a thickness $\delta d = d/N$ was assumed to be uniform and characterized by a local Jones matrix $\mathbf{J}_i\,(x, z_i)$, where subscript i denotes the i^{th} layer. Thus in each stripe, the total propagation matrix $\mathbf{J}(x)$ ($\mathbf{J}_{\mathrm{dark}}$ or $\mathbf{J}_{\mathrm{UV}}$ depending on the stripe) is a product of all $\mathbf{J}_i(x, z_i)$. Its characteristics can be numerically simulated.

In the 2D model, the director profile changes continuously also in the x direction. Thus, it is not enough to calculate only two Jones matrices for the two stripes, instead the total propagation matrix $\mathbf{J}(x)$ has to be independently calculated for each x position.

c) *Polarization state of the diffracted beam*

Being homogeneously illuminated by the probe beam with its electric field $\mathbf{E}_{\mathbf{in}}$, the electric field $\mathbf{E}_{\mathbf{out}}$ of the light exiting from the cell is obtained by using the total propagation matrix $\mathbf{J}(x)$:

$$\mathbf{E}_{\mathbf{out}}(x) = \mathbf{J}(x)\ \mathbf{E}_{\mathbf{in}} \qquad (2)$$

Due the sample's periodic deformation the exiting light suffers diffraction. Its characteristics can be obtained via a Fourier transformation with Fraunhofer and paraxial approximation; the far field diffraction properties are determined by the Fourier coefficients.

The diffracted electric field of order m can be expressed as follows [23-25]:

$$\mathbf{E}_{\mathrm{out},m} = \frac{1}{\Lambda}\int_0^{\Lambda} \mathbf{J}(\mathrm{x}) \cdot \mathbf{E}_{\mathrm{in}} \cdot e^{-i2\pi m x/\Lambda} dx \qquad (3)$$

As the incident field $\mathbf{E}_{\mathrm{in}}$ is independent of x, the far-field Fourier components can be written as:

$$\mathbf{E}_{\mathrm{out},m} = \mathbf{\Gamma}_m\,\mathbf{E}_{\mathrm{in}} \;\text{ where }\; \mathbf{\Gamma}_m = \frac{1}{\Lambda}\int_0^{\Lambda} \mathbf{J}(\mathrm{x})\; e^{-i\frac{2\pi}{\Lambda}mx}\,dx \quad (4)$$

Finally, the polarization state of the diffracted beam is determined from the amplitudes of the components of $\mathbf{E}_{\mathrm{out},m}$ and their phase difference.

In the 1D approximation, due to the binary periodic structure, $\mathbf{\Gamma}_m$ is composed of the contributions from $\mathbf{J}_{\mathrm{dark}}$ and $\mathbf{J}_{\mathrm{UV}}$ only:

$$\mathbf{\Gamma}_m = \frac{1}{\Lambda}\int_0^{\Lambda/2} \mathbf{J}_{\mathrm{dark}}\, e^{-i\frac{2\pi}{\Lambda}mx}\,dx + \frac{1}{\Lambda}\int_{\Lambda/2}^{\Lambda} \mathbf{J}_{\mathrm{UV}}\, e^{-i\frac{2\pi}{\Lambda}mx}\,dx \qquad (5)$$

We consider only the 1st order diffraction, which was found to dominate experimentally. Then $m = 1$ and Λ is one period, and Eq. (5) can be simplified as

$$\mathbf{\Gamma}_1 = -\left(\frac{\mathrm{i}}{\pi}\right)[\mathbf{J}_{\mathrm{dark}} - \mathbf{J}_{\mathrm{UV}}] \quad \text{yielding} \quad \mathbf{E}_{\mathrm{out},1} = \mathbf{\Gamma}_1\mathbf{E}_{\mathrm{in}} \qquad (6)$$

In the 2D approximation, $\mathbf{J}(x)$ varies continuously; therefore the complete definition in Eq. (4) should be used.

Figures 11(a)-11(c) compare the data calculated in the 1D and the 2D model, showing how the polarization angle β, the degree of linear polarization ($DoLP$) and the diffraction efficiency η of the ±1st order diffracted beams, respectively, vary with the pitch ratio $P(I_{\mathrm{uv}})/P_0$ in an initially left-handed sample of $\Phi_0 \approx -\frac{1}{2}\pi$. The curves reveal that all parameters depend on I_{uv} through $P(I_{\mathrm{uv}})$. In order to help comparison with the experiments in Figs. 5 and 6, we note that taking into account the strongly nonlinear relation $P(I_{\mathrm{uv}})$ between the pitch and the UV intensity [8], the range of $P(I_{\mathrm{uv}})/P_0$ used in the simulations roughly corresponds to the intensity range of $I_{\mathrm{uv}} > 3\,I_{\mathrm{c}}$.

It is clear that in the 1D approach the ±1st orders are identical; however, in the 2D approach all characteristics of the +1st and the -1st orders are significantly different, which we attribute to the asymmetry of the director profile. The calculations also revealed that in the 1D model the ±1st orders are dominant in the diffraction; in contrast to it, in the 2D model the ±2nd orders have the highest intensity. Experiments reveal strong 1st order diffraction spots with rapidly decaying intensity of the higher orders. The spots are slightly asymmetric resembling the results of the 2D model.

A full agreement between experimental and simulation data has not been achieved. A possible reason for the discrepancy could be that the Jones matrix method, which has been developed originally for stratified, laterally homogeneous systems, does not provide satisfactory data for laterally inhomogeneous, periodic systems. As the system exhibits strong optical anisotropy combined with significant x-dependent director gradients as seen in Fig. 9, one can expect strong light deflection (“mirage effect”), which is not accounted for in the frame of the Jones matrix method, where the light is assumed to propagate in straight columns along the z-direction. A more realistic description of the light propagation is a future task involving more advanced methods like Fourier optics or large-scale ab-initio numerical calculations based on the Maxwell equations. Implementation of the recent optical analysis of spatially periodic liquid crystal patterns [26] could provide more precise conclusions.

We hope that the proposed method could be optimized towards optical systems for polarization manipulation in the future.

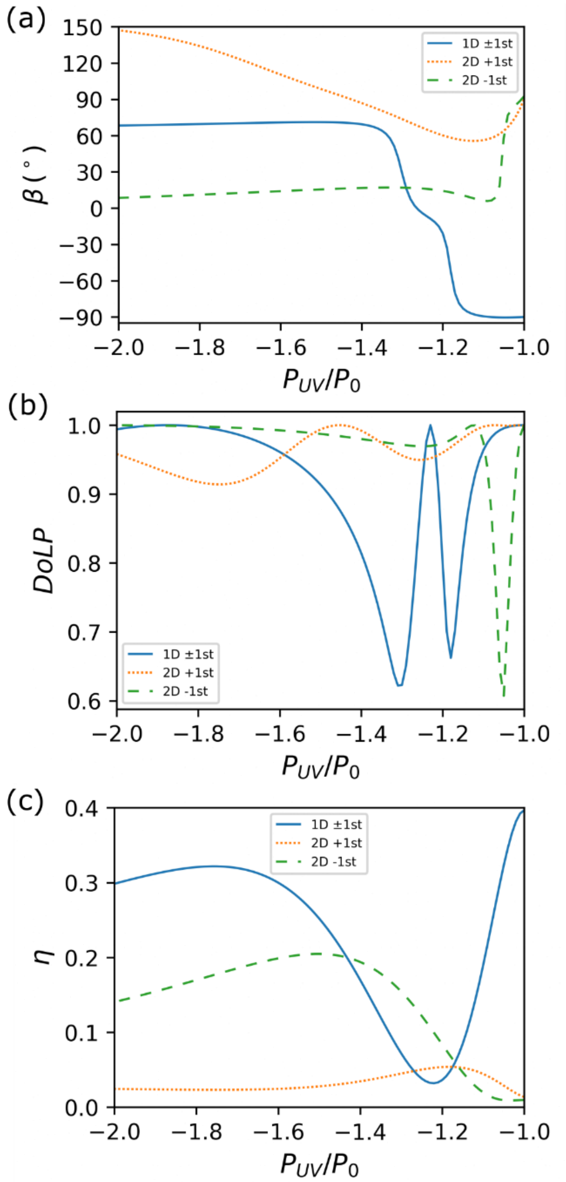

Figure 11. Simulation results demonstrating how (a) the polarization angle β, (b) the degree of linear polarization (*DoLP*) and (c) the diffraction efficiency of the 1st order diffracted beam varies with the pitch ratio $P(I_{uv})/P_0$ in an initially left-handed sample of $\Phi_0 \approx -\frac{1}{2}\pi$. The solid blue curve corresponds to the ±1st order in the 1D model, while the dotted red and the dashed green curves belong to the +1st and the -1st order in the 2D model.

5 Application scenarios

The above experimental results proved that the polarization state of the incident light could be modulated by UV light, thus our devices combining the self-assembling helical structure and the HAC cell geometry could work as polarization converters. Herein, by virtue of UV light with specific patterns, we present two proof-of-concept experiments demonstrating such potential applications.

5.1 Dynamic vortex light generator

Recently, light with an orbital angular momentum (OAM), accompanied by a spiral phase profile with the topological charge m, has attracted great interest [27]. Such optical fields, known as vortex beams, have triggered various applications including optical manipulation, laser manufacturing, sensing, and super-resolution imaging [28].

The helical wavefront of an optical vortex can generally be described by the phase function $\psi = e^{im\varphi}$, where φ is the azimuthal angle of a cylindrical coordinate system (r, φ, z) around the z axis that indicates the beam propagation direction, and m is the topological charge that can be positive or negative, depending on the direction of the twist (positive for counterclockwise rotation and negative for clockwise rotation). The phase singularity at the axis dictates zero intensity, which leads to a donut-like intensity distribution.

So far, several techniques were developed to generate optical vortices: one straightforward approach is a wave plate (Q-plate) with specified geometry of birefringence; another alternative choice is the “fork” grating, with dislocations centered in order to carry information of the topological charge. The fork grating can convert a Gaussian beam into a series of helically phased beams with opposite twist directions. Although at present fork grating is a quite convenient way to generate beam vortices, the geometry of such gratings are fixed, thereby their output topological charge cannot not be changed [29]. Thus, new alternative techniques for generating fast switchable and reconfigurable optical vortices, especially with tunable polarization and intensity, are highly desirable.

Specially designed computer-generated holograms [30], with fork morphologies corresponding to different topological charges, were transferred to our sample by DMD based microlithography. As a result, the incident Gaussian beam was transformed into vortices in the diffraction orders of the output beam.

The experiments, as shown in Fig. 12, indicated that under specially patterned UV light a fork grating can be formed in the self-induced helical structures. Thus a vortex beam generator was realized, which exhibited two peculiar advantages: ① it is reconfigurable, i.e., it is capable of online switching of the topological charge; ② it is tunable, i.e., it is capable of changing the polarization and intensity of the vortex beams.

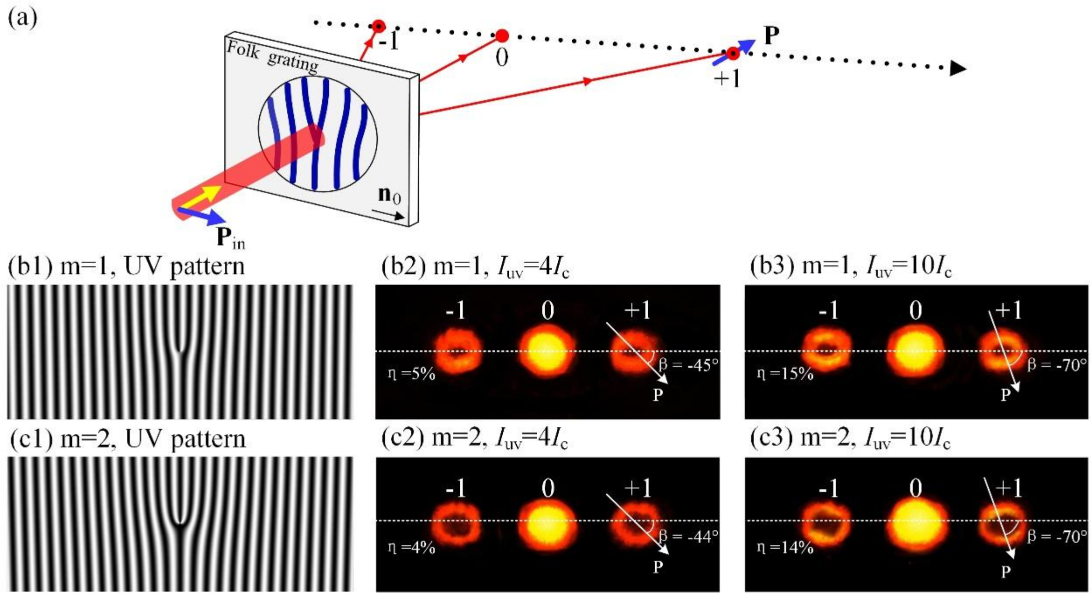

Figure 12. (a) Far-field Fraunhofer diffraction fringes of fork grating, each order being an optical vortex; (b1) Computer-generated holograms of fork grating with $m = 1$; (b2) and (b3) are diffraction fringes of (b1), with different linear polarization states and efficiencies according to the UV intensity; (c1), (c2), (c3) the topological charge reconfigured in situ, from $m = 1$ to $m = 2$.

5.2 Dynamic vector beams generator

Besides the vortex beams, vector beams, featured by spatially variant polarization states, have also gained considerable interest in fields including laser processing, nonlinear optics, and terahertz technology [31]. Usually, spatially varying phase retarders based on wave plates are adopted to convert homogeneously polarized beams into desired vector beams, however they can work for a specific wavelength only [32]. The interference of two orthogonally polarized beams from computer-generated holograms can be used as another method [33]; unfortunately, the generating efficiency is quite low. Furthermore, it should be noted that due to the constraint of their passive structure, currently most generators only output fixed vector beams, which makes the applications rather inflexible.

Herein we demonstrate a prototype to generate arbitrary vector beams, which may work in a dynamic manner. By adjusting specific UV intensity pattern online, an incident linearly polarized light could be transformed into a transmitted light with a custom made vector field. In Fig. 13, we present two examples: we show how to produce a basic radially or azimuthally polarized light field of circular symmetry. The merits of our devices were found as: ① they are reconfigurable, capable of online switching between different vector fields; ② they are achromatic, the generated vector fields are irrespective of the light wavelength.

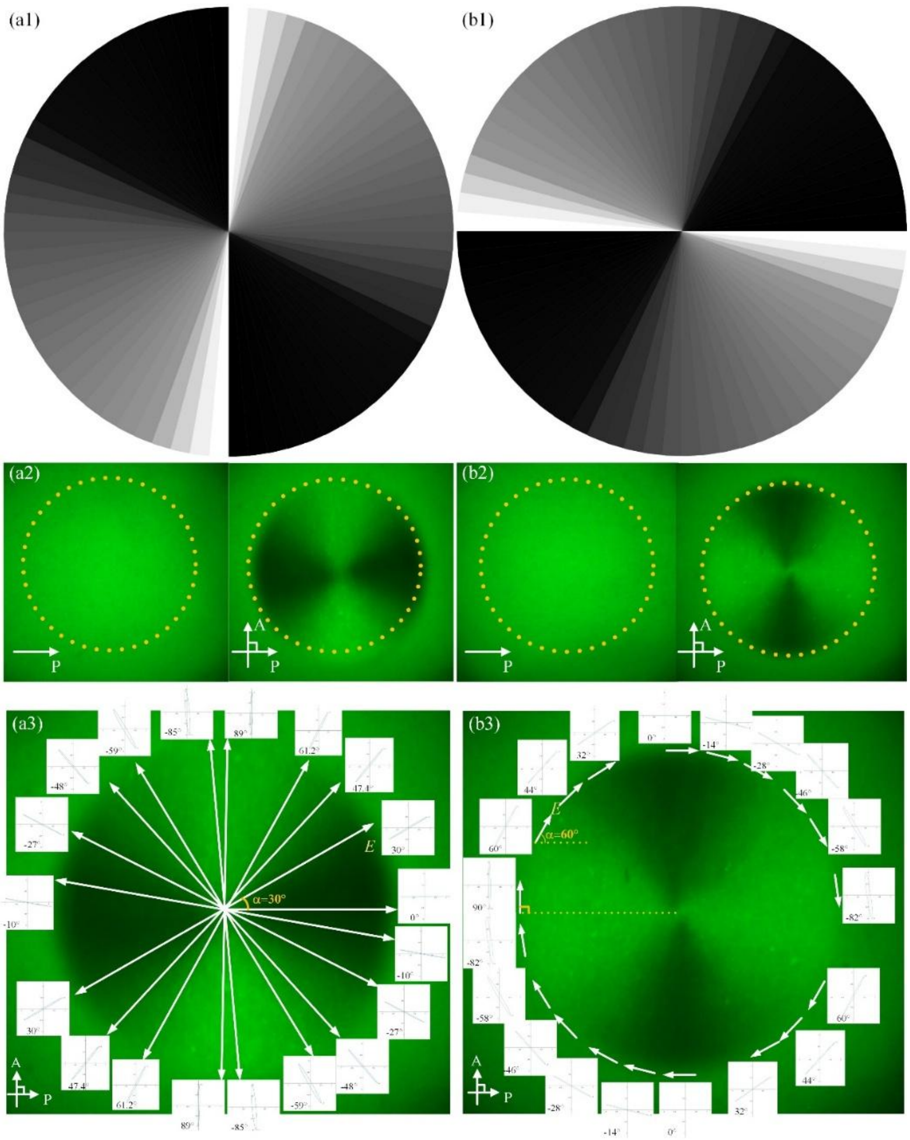

Figure 13. Dynamic vector beam generator, which modulates the incident light of wavelength λ = 532 nm with spatially uniform linear polarization, and outputs the transmitted light (a) as radial and (b) as azimuthal vector beams, respectively. Here (a1) and (b1) are the photomasks, (a2) and (b2) are the far-field beam morphologies without and with analyzer, (a3) and (b3) are spatial distribution of the linear polarization.

6 Conclusion

To summarize, a polarization rotator, based on a diffraction effect induced via photo-patterning of a photoresponsive CLC, was designed, fabricated and demonstrated. Depending on the UV intensity, the concentration and type of the photosensitive chiral dopant, the resulting rotation angle of linear polarization of the diffracted beam could be from $-\pi/2$ to $+\pi/2$, thereby covering the whole horizontal plane.

It should be stressed that this effect can work in a *dynamic manner*, i.e., specific gratings can be developed and reconfigured in real time according to customized UV patterns. The dynamic nature origins from a bulk effect, where the self-assembled helical superstructures are either compressed or dilated in response to the strength of the commanding UV field.

In addition, two innovative methods to customize dynamic vortex- and vector-light fields were proposed, which might promote cutting-edge applications in *in-situ* optical polarization manipulation.

Acknowledgments

This work was supported by Guangdong Provincial Science and Technology Plan (2022A1515010777 and 2022A0505050072); Hungarian National Research, Development, and Innovation Office under Grant NKFIH FK142643, EIG CONCERT-Japan project FerroFluid (2023-1.2.1-ERA_NET-2023-00008); Czech project, Czech Science Foundation (22-16499S); National Key R&D Program of China (2020YFE0100200), Science and Technology Projects in Guangzhou (202201000008) and Guangdong Provincial Key Laboratory of Optical Information Materials and Technology (2017B030301007); Fundamental Research Funds for the Central Universities (2023FRFK06011). PS was supported by the János Bolyai Research Scholarship of the Hungarian Academy of Sciences.

Conflict of Interest

The authors declare no conflict of interest.

References

[1] S. T. Wu and D. K. Yang, Reflective Liquid Crystal Displays (John Wiley & Sons, Ltd, 2001).

[2] W. Lee, and S. T. Wu, Focus issue introduction: liquid crystal materials for photonic applications, *Opt. Mater. Express* **1**, 1585-1587 (2011).

[3] J. Yan, Y. Li, and S. T. Wu, High-efficiency and fast-response tunable phase grating using a blue phase liquid crystal, *Opt. Lett.* **36**(8), 1404-1406 (2011).

[4] W. Hu, A. K. Srivastava, F. Xu, J. T. Sun, X. W. Lin, H. Q. Cui, V. Chigrinov, and Y. Q. Lu, Liquid crystal gratings based on alternate TN and PA photoalignment, *Opt. Express* **20**, 5384-5391 (2012).

[5] M. Y. Xu, H. Z. Jing, Y Xiang, Y. K. Liu, Z. G. Cai, F. J. Wang, J. Y. Li, E. Wang, Y. Q. Wang, and Y. H. Cai, Voltage selectable dual-mode optically induced grating in ZnTPP doped chiral nematic liquid crystals, *Opt. Mater. Express* **7**(4), 1317 (2017).

[6] J. Kim, J. H. Suh, B. Y. Lee, S. U. Kim, and S. D. Lee, Optically switchable grating based on dye-doped ferroelectric liquid crystal with high efficiency, *Opt. Express* **23**, 12619-12627 (2015).

[7] Y. H. Shin, Z. Y. Zhou, S. Halder, X. F. Zhang, D. K. Yang, Reconfigurable liquid crystal diffraction grating based on flexoelectric effect, *J. Mol. Liq.* **357**, 119150 (2022).

[8] H. Z. Jing, Y. Xiang, M. Y. Xu, Everett Wang, J. Wang, N. Éber, and Á. Buka, Light-Controllable Electroconvection Patterns in a Chiral Nematic Liquid Crystal, *Phys. Rev. Appl.* **10**, 014028 (2018).

[9] Y. Xiang, H. Z. Jing, Z. D. Zhang, W. J. Ye, M. Y. Xu, E. Wang, P. Salamon, N. Éber, and Á. Buka, Tunable Optical Grating Based on the Flexoelectric Effect in a Bent-Core Nematic Liquid Crystal, *Phys. Rev. Appl.* **7**, 064032 (2017).

[10] D. K. Yang, S. T. Wu, Fundamentals of liquid crystal devices, John Wiley & Sons (2014).

[11] V. S. Sutormin, M. N. Krakhalev, I. V. Timofeev, R. G. Bikbaev, O. O. Prishchepa, and V. YA. Zyryanov, Cholesteric layers with tangential-conical surface anchoring for an electrically controlled polarization rotator, *Opt. Mater. Express* **11**, 1527-1536 (2021).

[12] H. Ren, S. T. Wu, Liquid-crystal-based linear polarization rotator, *Appl. Phys. Lett.* **90** 121123 (2007).

[13] L. G. Hao, F. Liang, H. Jing, Y. Xiang, P. Salamon, N. Éber, Á. Buka, M. Kohout, J. Chen, and Y. Pei, Control of light polarization by optically-induced-chirality in photosensitive nematic fluids, *Opt. Express.*, **32**, 13965-13977 (2024).

[14] K. Yin, E. L. Hsiang, J. Zou, Y. Li, Z. Yang, Q. Yang, P.-C. Lai, C.-L. Lin, S.-T. Wu, Advanced liquid crystal devices for augmented reality and virtual reality displays: principles and applications, *Light Sci. Appl.* **11**, 161 (2022).

[15] J. H. Park, B. Lee, Holographic techniques for augmented reality and virtual reality near-eye displays, *LAM* **3**, 137-150 (2022).

[16] Y. Xiang, H. Z. Jing, W. Y. Sun, H. Chen, G. Cipparrone, P. Pagliusi, M. Xu, G. Huang, E. Wang, Topological defects arrays and control of electro-convections in periodically photo-aligned bent-core nematics, *J. Mol. Liq.* **318**, 114058 (2020).

[17] C. Provenzano, P. Pagliusi, G. Cipparrone. Highly efficient liquid crystal based diffraction grating induced by polarization holograms at the aligning surfaces, *Appl. Phys. Lett.* **89,** 121105 (2006).

[18] L. Nikolova and P. S. Ramanujam, *Polarization Holography* (Cambridge University Press, 2009).

[A] J. Sun, L. Yu, L. Wang, C. Li, Z. Yang, W. He, C. Zhang, L. Zhang, J. Xiao, X. Yuan, F. Lie, and H. Yang, Optical intensity-driven reversible photonic bandgaps in self-organized helical superstructures with handedness inversion, J. Mater. Chem. C **5**, 3678 (2017).

[B] Jane Cooper, Compositional Analysis of Merck E7 Liquid Crystal Intermediates Using UltraPerformance

Convergence Chromatography (UPC2) with PDA Detection, Application Note, Waters Corporation, (2003).
[C] Ana Mouquinho, Mara Saavedra, Alexandre Maiau, Krasimira Petrova, M. Teresa Barros, J. L. Figueirinhas, and Joao Sotomayor, Films Based on New Methacrylate Monomers: Synthesis, Characterisation and Electro-Optical Properties, *Mol. Cryst. Liq. Cryst.* **542**, 132–140 (2011).

~~[19] H. Z. Jing, Y. Xiang, M. Y. Xu, E. Wang, J. Wang, N. Éber, Buka, Ágnes, Light-H. Z. Jing, Y. Xiang, M. Y. Xu, E. Wang, J. Wang, N. Éber, Buka, Ágnes, Light-controllable electroconvection patterns in a chiral nematic liquid crystal, *Phys. Rev. Appl*. **10(1)**, 014028 (2018).~~

[20] Y. Xiang, H. Z. Jing, H. Chen, J. Zhang, X. Y. Ding, J. Y. Li, Z. G. Cai, N. Éber, Á. Buka, Light-driven rotation of gratings formed by electroconvection patterns in cholesteric liquid crystals, *J. Mol. Liq*. **337**, 116366 (2021).

[21] H. Wu, W. Hu, H. C. Hu, X. Lin, G. Zhu, J.-W. Choi, V. Chigrinov, and Y. Lu, Arbitrary photo-patterning in liquid crystal alignments using DMD-based lithography system, *Opt. Express* **20(15)**, 16684-16689 (2012).

[22] D. S. Kliger, J. W. Lewis, and C. Einterz Randall, *Polarized Light in Optics and Spectroscopy* (Academic Press, 1990).

[23] L. Tan, J. Y. Ho, H.-S. Kwok, Extended Jones matrix method for oblique incidence study of polarization gratings, *Appl. Phys. Lett*. **101**, 051107 (2012).

[24] W. Chen, Z. Zhao, C. Wang, H. Li, R. Wei, S. Zhang, Z. Peng, Y. Liu, Q. Wang, Q. Mu, L. Xuan, Linear polarization grating combining a circular polarization grating with a special cycloidal diffractive quarter waveplate, *Opt. Express* **27(23)**, 33378-3339 (2019).

[25] T. Zhan, J. Xiong, G. Tan, S.-T. Wu, Absorption-based polarization gratings, *Opt. Express* **28(9)**, 13907-13912 (2020).

[26] W. Pesch, A. Krekhov, Optical analysis of spatially periodic patterns in nematic liquid crystals: Diffraction and shadowgraphy, *Phys. Rev. E* **87**, 52504 (2013).

[27] Y. J.Shen, X. J.Wang, Z. W.Xie, C. J.Min, X.Fu, Q.Liu, M. L.Gong, X. C.Yuan, Optical Vortices 30 years on: OAM Manipulation from Topological Charge to Multiple Singularities, *Light Sci. Appl*. **8**, 90 (2019).

[28] Y. H. Zhang, P. Chen, C. T. Xu, L. Zhu, X. Y. Wang, S. J. Ge, W. Hu, Y. Q. Lu, Dynamically Selective and Simultaneous Detection of Spin and Orbital Angular Momenta of Light with Thermoresponsive Self-Assembled Chiral Superstructures, *ACS Photonics* **27**, 1050−1057 (2022).

[29] B. Y. Wei, W. Hu, Y. Ming, F. Xu, S. Rubin, J. G. Wang, V. Chigrinov, Y. Q. Lu, Generating Switchable and Reconfigurable Optical Vortices via Photopatterning of Liquid Crystals, *Adv. Mater*. **26**, 1590–1595 (2014).

[30] A. V. Carpentier , H. Michinel , J. R. Salgueiro , D. Olivieri , *Am. J. Phys.* **76**, 916 (2008).

[31] X. Y. Fan, W. Y. Ma, Y. M. Zhang, C. T. Xu, H. Ren, W. M. Han, C. Y. Chen, W. Hu, Broadband spatial polarization processing of light via a photopatterned dichroic medium, *Appl. Phys. Lett*. **120**, 041103 (2022).

[32] P. Chen, W. Ji, B. Y. Wei, W. Hu, V. Chigrinov, Y. Q. Lu, Generation of arbitrary vector beams with liquid crystal polarization converters and vector-photoaligned q-plates, *Appl. Phys. Lett.* **107**, 241102 (2015).

[33] Z. Lyu, C. Wang, Y. Yang, R. Xia, Polarization modulation by means of tunable polarization gratings in an azobenzene side-chain liquid-crystalline polymer film, *Appl. Opt*. **57**, 3146-3153 (2018)